ACS Catalysis

pubs.acs.org/acscatalysis Letter

Active Site Isolation and Enhanced Electron Transfer Facilitate Photocatalytic CO_2 Reduction by A Multifunctional Metal−Organic Framework

Zitong Wang, Pierce Yeary, Yingjie Fan, Chenghua Deng, and Wenbin Lin*

Cite This: *ACS Catal.* 2024, 14, 9217−9223 Read Online

ABSTRACT: We report a multifunctional metal−organic framework (MOF) photocatalyst for the CO_2 reduction reaction (CO_2RR) under visible light irradiation with high efficiency (turnover number = 2638) and CO selectivity (97.0%). The short distance (6.6 Å) between bipyridine sites in the MOF allows the integration of Ir photosensitizers and Ni catalysts in proximity, thereby enhancing their electron transfer for photocatalytic CO_2RR. Isolation of these metal centers by the MOF structure prevents their deactivation, leading to 54 times higher CO_2RR activity than the homogeneous system and allowing for easy recovery for use in five consecutive cycles of photocatalytic CO_2RR without significant loss of catalytic activity.

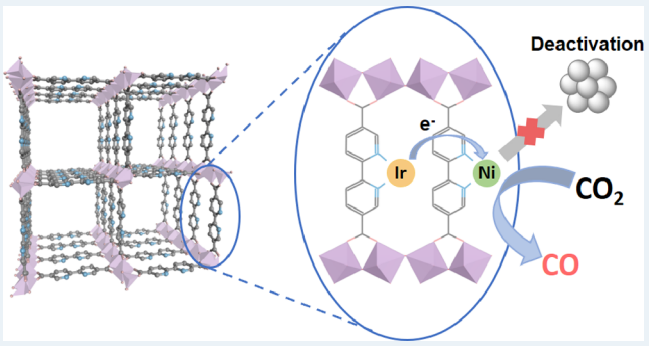

KEYWORDS: *metal−organic framework, heterogeneous photocatalysis, CO_2 photoreduction, site isolation, synergistic catalysis*

Carbon dioxide (CO_2) reduction reaction (CO_2RR) to CO represents a sustainable strategy to generate value-added chemical feedstocks and chemical energy supplies from greenhouse gases and can positively contribute to mitigating climate change caused by the overexploitation of fossil fuels.[1−3] In a photocatalytic CO_2RR, a photosensitizer harvests light energy to enable electron transfer to a catalyst for CO_2 conversion to chemical feedstocks or fuels.[4−7] However, the efficiency of photocatalytic CO_2RR is limited by suboptimal energy and electron transfer between the molecular photosensitizing and catalytic units. Bifunctional molecular systems with both photosensitizing and catalytic units can potentially address this limitation, but their synthesis remains a significant challenge. Moreover, as photocatalytic CO_2RR is performed by metal centers at low oxidation states,[8−11] the active sites can readily deactivate via multimolecular aggregation or formation of metallic nanoparticles, which further limits the practical application of photocatalytic CO_2RR in sustainable chemical feedstock production and solar energy conversion.[12,13]

As an emerging class of crystalline molecular materials with high porosity, metal−organic frameworks (MOFs) can incorporate a wide variety of catalytically active species on the periodically repeating nodes and organic linkers to catalyze synthetically useful organic transformations.[14−17] The isolation of catalytic sites by the framework inhibits deactivation pathways to enhance the stability of active catalysts.[18−25] By taking advantage of their synthetic versatility, many MOFs with multiple active species have also been developed to synergistically combine different functions.[26−31] These features have spurred the development of MOFs as efficient photocatalysts for the synthesis of chemical feedstocks and in solar energy conversion.[15,32−55]

Herein, we report the design and synthesis of a multifunctional MOF with hierarchically integrated Ir photosensitizers (Ir-PSs) and bipyridine-coordinated Ni(II) catalytic centers to achieve photocatalytic CO_2RR with high efficiency and CO selectivity. The close distance between adjacent bipyridyl linkers (6.6 Å) facilitates electron transfer, which enhances the overall efficiency of the photocatalytic process; additionally, the inhibition of catalyst deactivation caused by aggregation and the formation of nanoparticles by the isolation of active sites in the framework further enhances the photocatalytic efficiency. These advantages of MOFs have endowed simple bipyridyl−nickel complexes as efficient catalysts for CO_2RR.

The photocatalytic **MOF-253-Ir/Ni** was synthesized via multiple-step postsynthetic modifications (PSMs) of the previously reported MOF-253.[56−60] A solvothermal reaction between $Al(NO_3)_3{\cdot}9H_2O$ and 2,2′-bipyrdine-5,5′-dicarboxylic acid (H_2bpydc) in *N,N*-dimethylformamide (DMF) at 120 °C produced MOF-253 as a crystalline white powder. MOF-253

Received: April 19, 2024
Revised: May 23, 2024
Accepted: May 29, 2024
Published: June 3, 2024

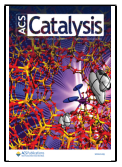

https://doi.org/10.1021/acscatal.4c02326
ACS Catal. 2024, 14, 9217−9223

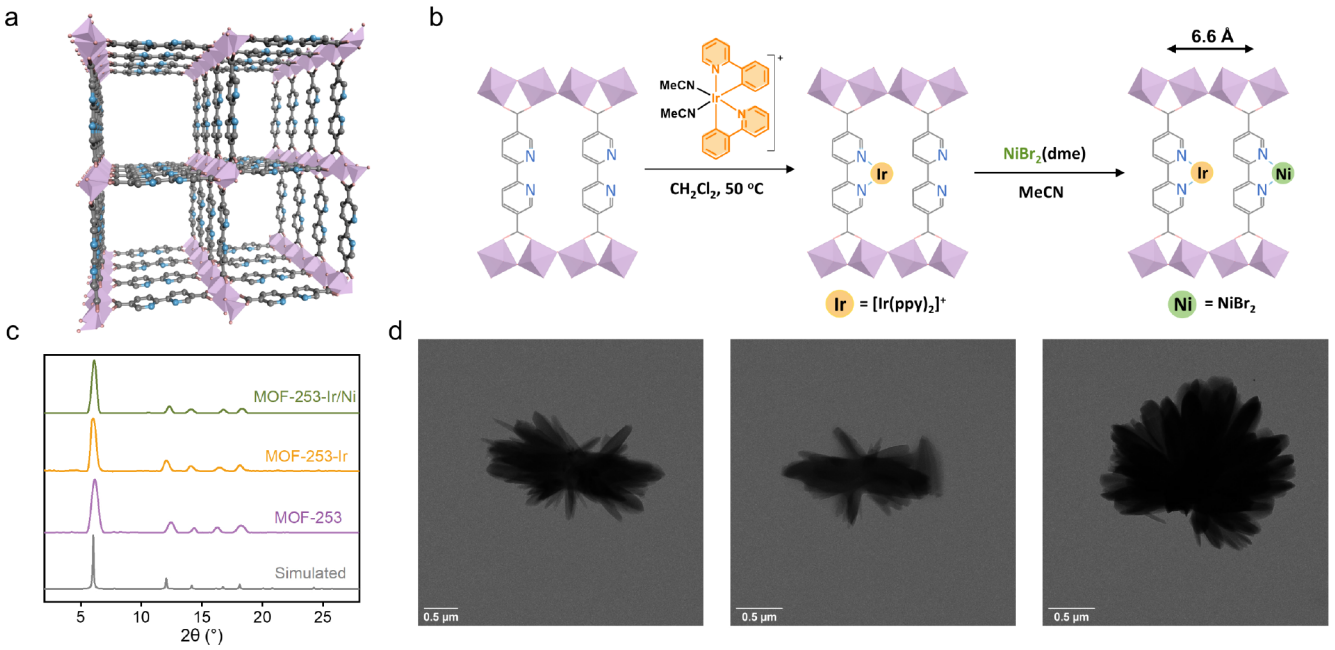

Figure 1. (a) Structural model of MOF-253 showing a parallel arrangement of closely spaced bipyridyl linkers. (b) Stepwise metalation of the bpy sites in MOF-253 for the construction of the multifunctional photocatalyst **MOF-253-Ir/Ni**. (c) PXRD patterns of MOF-253 (purple), **MOF-253-Ir** (yellow), and **MOF-253-Ir/Ni** (green), along with the simulated pattern for MOF-253. (d) TEM images of MOF-253 (left), **MOF-253-Ir** (middle), and **MOF-253-Ir/Ni** (right).

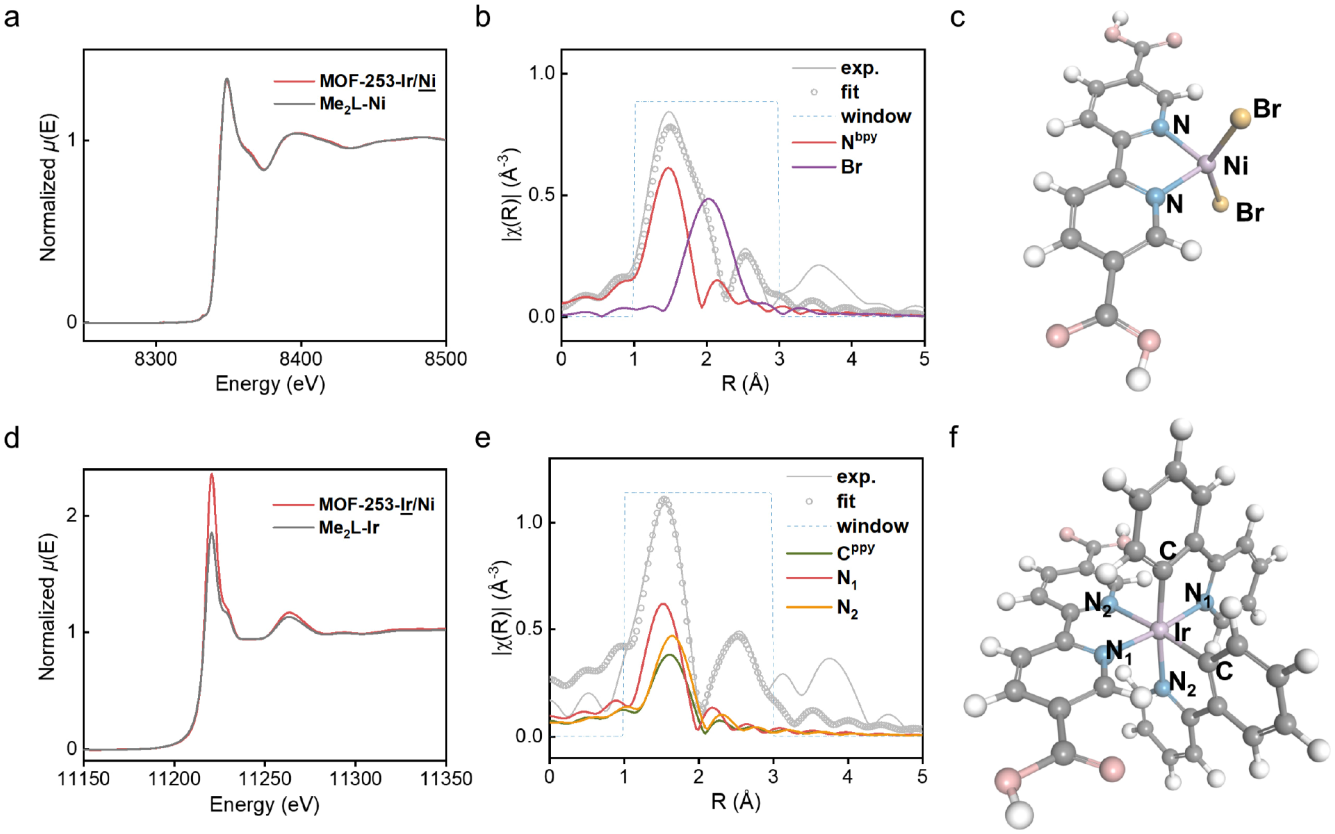

Figure 2. (a) Normalized Ni K-edge XAS spectra of **MOF-253-Ir/Ni** (red line) and **Me$_2$L-Ni** (gray line). (b) EXAFS spectrum and fit in *R*-space at Ni K-edge of **MOF-253-Ir/Ni**, as well as the contribution of different scatterers in the first coordination sphere. (c) Structural model of the Ni site (d) Normalized Ir L$_3$-edge XAS spectra of **MOF-253-Ir/Ni** (red line) and **Me$_2$L-Ir** (gray line). (e) EXAFS spectrum and fit in *R*-space at the Ir L$_3$-edge of **MOF-253-Ir/Ni**, as well as the contribution of different scatterers in the first coordination sphere. (f) Structural model of the Ir site.

was chosen as the platform for photocatalyst construction because of the closely spaced bipyridine (bpy) linkers and their parallel arrangement, which was expected to enhance electron transfer in the CO_2RR process (Figure 1a).

https://doi.org/10.1021/acscatal.4c02326
ACS Catal. 2024, 14, 9217−9223

As shown in Figure 1b, **MOF-253-Ir/Ni** was synthesized via stepwise metalation of MOF-253. After treatment of MOF-253 with $[Ir(ppy)_2(MeCN)_2]PF_6$ in dichloromethane for 48 h, the white powder turned orange, suggesting the successful installation of Ir-PSs via coordination of Ir centers to the bpy sites of MOF-253 to obtain **MOF-253-Ir**. The ^{1}H NMR spectrum of digested **MOF-253-Ir** demonstrated 10% loading of $[Ir(ppy)_2]$ in MOF-253, which shows complete coordination of the $[Ir(ppy)_2(MeCN)_2]PF_6$ precursor. The remaining bpy sites (90%) in **MOF-253-Ir** were subsequently converted to $(bpy)NiBr_2$ via treatment with $Ni(dme)Br_2$ (dme = 1,2-dimethoxyethane) to afford **MOF-253-Ir/Ni**. Inductively coupled plasma mass spectrometric (ICP-MS) analysis of **MOF-253-Ir/Ni** showed a Ni/Al ratio of 0.9 consistent with complete coordination of Ni to the bpy sites in **MOF-253-Ir**.

Powder X-ray diffraction (PXRD) experiments showed that the crystallinity of MOF-253 was retained after postsynthetic installation of Ir-PS and bpy-$NiBr_2$ moieties (Figure 1c). Transmission electron microscopy (TEM) revealed that the rodlike morphology of MOF-253 remained unchanged throughout stepwise metalation processes (Figure 1d). Thermogravimetric analysis (TGA) supported the chemical compositions of the synthesized MOF-253, **MOF-253-Ir**, and **MOF-253-Ir/Ni** as Al(OH)(bpydc), Al(OH)(bpydc)$[Ir(ppy)_2PF_6]_{0.1}$, and Al(OH)(bpydc)$[Ir(ppy)_2PF_6]_{0.1}(NiBr_2)_{0.9}$, respectively (Figures S6, S10, and S12). N_2 sorption isotherms demonstrated a decrease of Brunauer−Emmett−Teller surface area from 1576 ± 35 m^2/g for MOF-253 to 1033 ± 26 m^2/g for **MOF-253-Ir** and 400 ± 8 m^2/g for **MOF-253-Ir/Ni** (Figures S7, S11, and S13), which is consistent with the introduction of bulky Ir-PSs and bpy-$NiBr_2$ moieties upon sequential metalation of the bpy sites in MOF-253. Fourier transform infrared (FT-IR) spectra of MOF-253, **MOF-253-Ir**, and **MOF-253-Ir/Ni** were compared. After Ir installation, a new peak appeared at 1696 cm^{-1} with a low intensity because of a low loading (10%) of Ir. Comparisons of the FT-IR spectra of **MOF-253-Ir** and **MOF-253-Ir/Ni** showed peak changes at 1700−1300 cm^{-1} due to the bpy conformational change from *trans* to *cis* after Ni loading.[61] All new peaks can be found in the FTIR spectra of homogeneous model complexes $(Me_2bpydc)Ir(ppy)_2PF_6$ (**Me_2L-Ir**) and $(Me_2bpydc)NiBr_2$ (**Me_2L-Ni**).

X-ray absorption spectroscopy (XAS) was used to probe the oxidation states and coordination environments of photosensitizing Ir centers and catalytic Ni centers in **MOF-253-Ir/Ni**. Both **MOF-253-Ir/Ni** and the homogeneous model complex **Me_2L-Ni** showed a Ni K-edge energy of 8343.4 eV (Figure 2a−c), which is within the reported range for Ni(II). This result demonstrated a +2 oxidation state for the Ni centers in **MOF-253-Ir/Ni**.[62] Moreover, **MOF-253-Ir/Ni** exhibited an almost identical X-ray absorption spectrum at the Ni K-edge as **Me_2L-Ni**, thereby suggesting their similar Ni(II) coordination environments. Extended X-ray absorption fine structure (EXAFS) analysis showed strong Ni−N_{bpy} and Ni−Br single scattering signals, which suggested coordination of the Ni(II) center to the two nitrogen atoms of the bpydc linker and two bromine atoms. Fitting of the EXAFS data to the DFT-optimized structural model gave Ni−N_{bpy} and Ni−Br bond lengths of 2.06 and 2.34 Å, respectively. **MOF-253-Ir/Ni** and **Me_2L-Ir** showed similar Ir L_3-edge values of 11218.0 and 11217.5 eV (Figure 2d−f), respectively, which indicated a +3 oxidation state for the Ir centers.[63,64] The peak intensity difference is likely caused by slight distortion of the bulky Ir moiety in the MOF due to steric hindrance. EXAFS analysis and fitting to the DFT-optimized model indicated the coordination of Ir(III) centers to one bpy and two ppy ligands with Ir−C and Ir−N bond distances of 2.03 and 2.07/2.18 Å, respectively. These results show that the Ir and the Ni centers in **MOF-253-Ir/Ni** exhibit the same oxidation states and coordination environments as their homogeneous model complexes.

With photosensitizing Ir(III) and catalytic Ni(II) centers in close proximity in **MOF-253-Ir/Ni**, we tested its performance as a photocatalyst in the CO_2RR. A Xe lamp with a 300 nm cutoff was used as the light source, and acetonitrile was used as the solvent for the CO_2RR. After the optimization of reaction conditions, we found that **MOF-253-Ir/Ni** efficiently promoted CO_2RR with 1,3-dimethyl-2-phenyl-2,3-dihydro-1*H*-benzo[*d*]imidazole (BIH) as a sacrificial agent to afford an outstanding turnover number (TON) of 2638 and a high CO selectivity of 97% (Figure 3a). Only trace amounts of H_2 and CH_4 were detected as byproducts of the CO_2RR by gas chromatography (GC), and no formic acid was detected by NMR after the CO_2RR (Figure S22). A control experiment with a N_2 atmosphere showed negligible CO generation, which excluded the possibility of CO generation from the decomposition of the catalyst or the solvent. Additionally, isotope tracer experiments using $^{13}CO_2$ gave ^{13}CO as the only product, thereby indicating that CO was generated from the photoreduction of CO_2 (Figure S24).

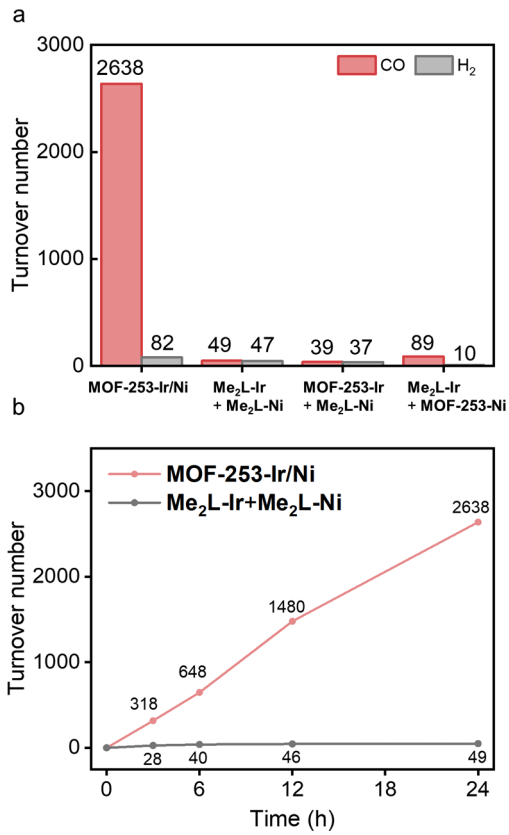

Figure 3. (a) Photocatalytic production of CO and H_2 by **MOF-253-Ir/Ni**, **Me_2L-Ir** plus **Me_2L-Ni**, **MOF-253-Ir** plus **Me_2L-Ni**, and **MOF-253-Ni** plus **Me_2L-Ir**. (b) Time-dependent CO TONs of **MOF-253-Ir/Ni** and **Me_2L-Ir** plus **Me_2L-Ni** homogeneous control.

https://doi.org/10.1021/acscatal.4c02326
ACS Catal. 2024, 14, 9217−9223

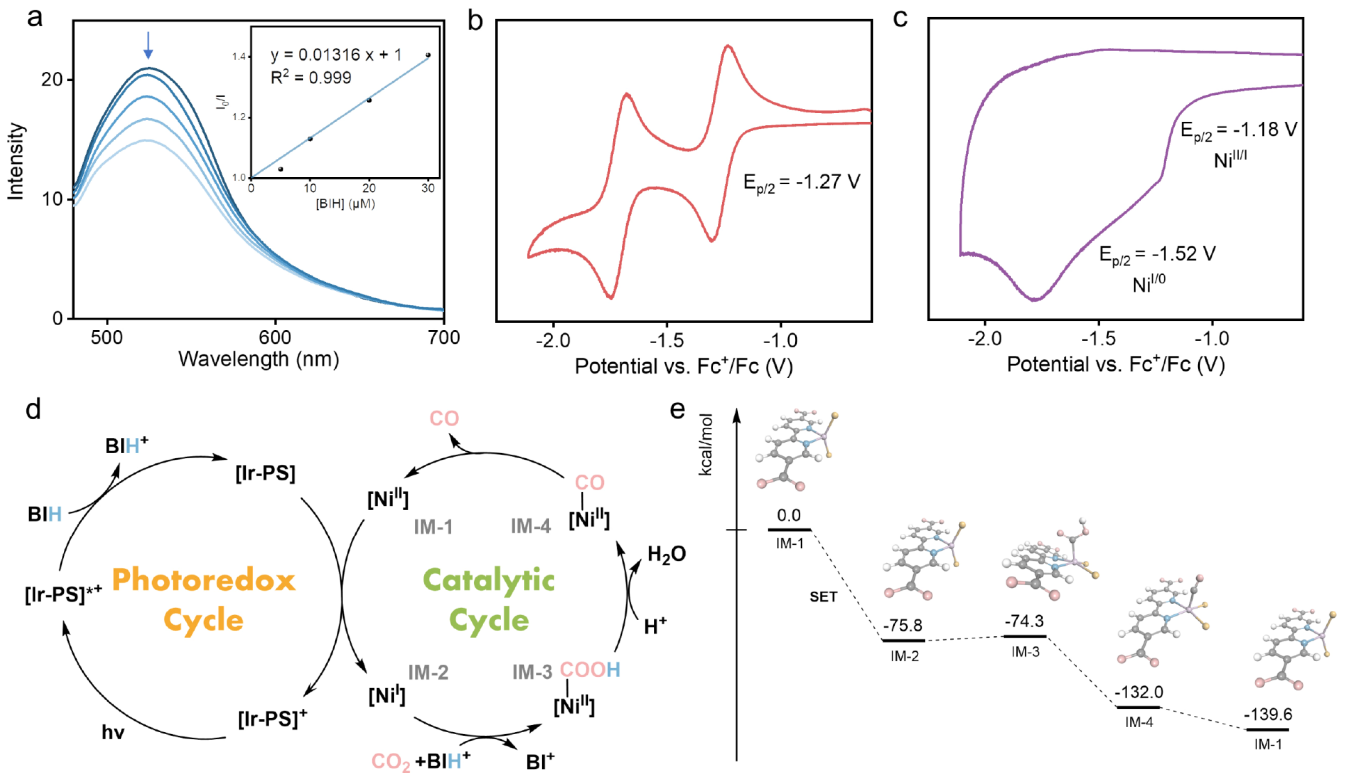

Figure 4. (a) Emission spectra of **Me$_2$L-Ir** (30 μM) after the addition of different amounts of BIH (From top to bottom: 0, 5, 10, 20, 30 μM), with the linear fitting giving a Stern−Völmer quenching constant of (13.2 ± 0.5) × 10^3 M^{-1}. (b,c) CVs of **Me$_2$L-Ir** (b) and **Me$_2$L-Ni** (c) in acetonitrile. (d) Proposed mechanism of **MOF-253-Ir/Ni**-catalyzed CO_2RR with CO as the product. (e) DFT-calculated energy profiles of the Ni cycle of **MOF-253-Ir/Ni**-catalyzed CO_2RR.

We conducted a series of control experiments to demonstrate CO_2RR enhancement via hierarchical integration of Ir photosensitizers and Ni catalytic centers in the MOF. Under the same conditions, a mixture of homogeneous **Me$_2$L-Ir** and **Me$_2$L-Ni** at the same Ir and Ni loadings as **MOF-253-Ir/Ni** showed a TON of 49 and CO selectivity of 51%. Thus, **MOF-253-Ir/Ni** outperformed its homogeneous control by 54-folds. Changing the photosensitizer from homogeneous **Me$_2$L-Ir** to **MOF-253-Ir** further decreased the TON to 39, likely because of less efficient electron transfer between **Me$_2$L-Ni** and the Ir-PS in the MOF. Using a combination of **MOF-253-Ni** and Me$_2$L-Ir as catalysts, the TON (CO) was determined to be 89, which was also significantly lower than that of **MOF-253-Ir/Ni**. This result further supported enhanced electron transfer in the bifunctional MOF catalyst. MOF-253 and **MOF-253-Ir** gave lower TONs of 29 and 26, respectively, indicating the important role of the Ni catalyst in photocatalytic CO_2RR. Time-dependent CO_2RR experiments showed that the catalytic performance of the homogeneous control decreased significantly over time and leveled off after the first 6 h with a TON of 40, which indicated rapid catalyst deactivation in the homogeneous system (Figure 3b). In contrast, **MOF-253-Ir/Ni** showed unchanged CO generation rate in 24 h, which demonstrated stabilization of both Ir-PS and Ni catalyst in the MOF via site isolation. The durability of **MOF-253-Ir/Ni** was further demonstrated by a nearly constant catalytic performance in five runs of the CO_2RR (Figure S23).

Photophysical and electrochemical experiments were conducted to probe the mechanism of the **MOF-253-Ir/Ni**-catalyzed CO_2RR. First, **MOF-253-Ir** displayed increased absorption at 350−450 nm over MOF-253 (Figure S25). This absorption is similar to that of **Me$_2$L-Ir**, which suggests the retention of the photosensitizing ability of Ir-PS upon installation in the MOF. A luminescence quenching experiment was next conducted to probe the interaction between photoexcited Ir-PS and the sacrificial agent. Luminescence measurements showed that the emission of Ir-PS was quenched by BIH, which was well fitted with the Stern−Völmer equation to give a quenching constant (K_{SV}) of (13.2 ± 0.5) × 10^3 M^{-1} (Figure 4a). This indicates that the excited state of Ir-PS can be reduced by BIH to generate the $(bpy^{\cdot-})Ir(ppy)_2$ species, which then injects electrons into the adjacent Ni catalytic centers for the CO_2RR.

Cyclic voltammograms (CVs) of **Me$_2$L-Ir** and **Me$_2$L-Ni** were examined to further support electron transfer between the $(bpy^{\cdot-})Ir(ppy)_2$ and Ni(II) centers in the MOF. CV scans of **Me$_2$L-Ir** in acetonitrile showed two reduction peaks with $E_{p/2}$ = −1.27 and −1.71 V vs Fc^+/Fc (Figure 4b), which were assigned to the $bpy^{0/-}$ and $ppy^{-/-2}$ redox couples.[65] **Me$_2$L-Ni** displayed irreversible peaks at $E_{p/2}$ = −1.18 and −1.52 V vs Fc^+/Fc (Figure 4c) corresponding to the $Ni^{II/I}$ and $Ni^{I/0}$ redox couples. These redox potentials demonstrate that the reduced Ir-PS $[(bpy^{\cdot-})Ir(ppy)_2]$ can undergo single electron transfer to reduce Ni(II) to Ni(I) but it cannot further reduce Ni(I) to Ni(0). Under a CO_2 atmosphere, the reduction current clearly increased, which supports the reduction of CO_2 by Ni(I) centers (Figure S26).

Based on the photophysical and electrochemical experimental results, we propose the following mechanism for **MOF-253-Ir/Ni**-catalyzed CO_2RR (Figure 4d). The Ir-PS is first photoexcited and reduced by BIH to generate $(bpy^{\cdot-})$-

https://doi.org/10.1021/acscatal.4c02326
ACS Catal. 2024, 14, 9217−9223

$Ir(ppy)_2$ and BIH^+. The proximity of the Ir-PS and Ni centers facilitates electron transfer from $(bpy\cdot^-)Ir(ppy)_2$ to the nearby Ni(II) center to generate the Ni(I) species, which binds CO_2 and undergoes proton-coupled electron transfer (PCET) with BIH^+ to generate a Ni(II)−COOH species, which is the key intermediate in the CO production pathway. The acid−base reaction of Ni(II)−COOH with proton generates the Ni(II)−CO intermediate and H_2O. Dissociation of CO from the Ni(II) center produces CO as the final product and regenerates the Ni(II) catalyst. Ir-PS mediated photosensitization cycle and Ni-mediated catalytic cycle are effectively coupled to enhance electron transfer in the MOF. DFT calculations with the B3LYP functional were conducted to determine the feasibility of the proposed mechanism from the perspective of free energy changes. The electron injection from $(bpy\cdot^-)Ir(ppy)_2$ to Ni(II) causes a free energy decrease of 75.8 kcal/mol (Figure 4e). The free energy changes for the subsequent CO_2 binding/PCET step, acid−base reaction step, and CO release step are 1.5, −57.7, and −7.6 kcal/mol, respectively. These calculation results support the feasibility of the proposed CO_2RR mechanism.

In summary, we rationally constructed multifunctional **MOF-253-Ir/Ni** with hierarchically assembled photosensitizing Ir centers and catalytic Ni centers via stepwise postsynthetic metalation of MOF-253. The proximity between adjacent Ir-PS units and catalytic Ni centers enhanced electron transfer to boost photocatalytic CO_2RR. Simultaneously, the active sites were isolated from each other in the MOF to prevent undesired deactivation under the CO_2RR conditions. As a result, **MOF-253-Ir/Ni** showed excellent CO_2RR activity under visible light irradiation with a TON of 2638 and a CO selectivity of 97.0%. This catalytic activity is 54 times higher than that of the homogeneous control. This work highlights the potential of MOFs as a tunable platform to construct multifunctional catalysts for photocatalysis and solar energy conversion.

■ ASSOCIATED CONTENT

Supporting Information

The Supporting Information is available free of charge at The Supporting Information is available free of charge at https://pubs.acs.org/doi/10.1021/acscatal.4c02326.

Materials and methods, synthesis and characterization of complexes and materials, details of visible-light-drive CO_2RR and photophysical and electrochemical experiments, computational studies, and additional references (PDF)

■ AUTHOR INFORMATION

Corresponding Author

Wenbin Lin − *Department of Chemistry, The University of Chicago, Chicago, Illinois 60637, United States;* orcid.org/0000-0001-7035-7759; Email: wenbinlin@uchicago.edu

Authors

Zitong Wang − *Department of Chemistry, The University of Chicago, Chicago, Illinois 60637, United States;* orcid.org/0000-0001-7883-5276

Pierce Yeary − *Department of Chemistry, The University of Chicago, Chicago, Illinois 60637, United States*

Yingjie Fan − *Department of Chemistry, The University of Chicago, Chicago, Illinois 60637, United States;* orcid.org/0000-0003-1857-5788

Chenghua Deng − *Department of Chemistry, The University of Chicago, Chicago, Illinois 60637, United States*

Complete contact information is available at: https://pubs.acs.org/10.1021/acscatal.4c02326

Notes

The authors declare no competing financial interest.

■ ACKNOWLEDGMENTS

This work was supported by NSF (CHE-2102554) and the University of Chicago. XAS analysis was performed at Beamline 10-BM and supported by the Materials Research Collaborative Access Team (MRCAT). Use of the Advanced Photon Source, an office of Science User Facility operated for the U.S. DOE office of Science by ANL, was supported by the U.S. DOE under contract DE-AC02-06CH11357. We thank Dr. Ningxin Jiang and Dr. Lei Wang at the University of Chicago for experimental help on surface area measurements.

■ REFERENCES

(1) Kondratenko, E. V.; Mul, G.; Baltrusaitis, J.; Larrazábal, G. O.; Pérez-Ramírez, J. Status and perspectives of CO2 conversion into fuels and chemicals by catalytic, photocatalytic and electrocatalytic processes. *Energy Environ. Sci.* **2013**, *6* (11), 3112−3135.

(2) Aresta, M.; Dibenedetto, A.; Angelini, A. Catalysis for the Valorization of Exhaust Carbon: from CO2 to Chemicals, Materials, and Fuels. Technological Use of CO2. *Chem. Rev.* **2014**, *114* (3), 1709−1742.

(3) Olah, G. A.; Prakash, G. K. S.; Goeppert, A. Anthropogenic Chemical Carbon Cycle for a Sustainable Future. *J. Am. Chem. Soc.* **2011**, *133* (33), 12881−12898.

(4) Barber, J. Photosynthetic energy conversion: natural and artificial. *Chem. Soc. Rev.* **2009**, *38* (1), 185−196.

(5) Wang, Y.; Chen, E.; Tang, J. Insight on Reaction Pathways of Photocatalytic CO2 Conversion. *ACS Catal.* **2022**, *12* (12), 7300−7316.

(6) Wagner, A.; Sahm, C. D.; Reisner, E. Towards molecular understanding of local chemical environment effects in electro- and photocatalytic CO2 reduction. *Nat. Catal.* **2020**, *3* (10), 775−786.

(7) Azcarate, I.; Costentin, C.; Robert, M.; Savéant, J.-M. Dissection of Electronic Substituent Effects in Multielectron-Multistep Molecular Catalysis. Electrochemical CO2-to-CO Conversion Catalyzed by Iron Porphyrins. *J. Phys. Chem. C* **2016**, *120* (51), 28951−28960.

(8) Kamada, K.; Jung, J.; Wakabayashi, T.; Sekizawa, K.; Sato, S.; Morikawa, T.; Fukuzumi, S.; Saito, S. Photocatalytic CO2 Reduction Using a Robust Multifunctional Iridium Complex toward the Selective Formation of Formic Acid. *J. Am. Chem. Soc.* **2020**, *142* (23), 10261−10266.

(9) Lee, S. K.; Kondo, M.; Okamura, M.; Enomoto, T.; Nakamura, G.; Masaoka, S. Function-Integrated Ru Catalyst for Photochemical CO2 Reduction. *J. Am. Chem. Soc.* **2018**, *140* (49), 16899−16903.

(10) Ha, E.-G.; Chang, J.-A.; Byun, S.-M.; Pac, C.; Jang, D.-M.; Park, J.; Kang, S. O. High-turnover visible-light photoreduction of CO2 by a Re(i) complex stabilized on dye-sensitized TiO2. *Chem. Commun.* **2014**, *50* (34), 4462−4464.

(11) Son, H.-J.; Pac, C.; Kang, S. O. Inorganometallic Photocatalyst for CO2 Reduction. *Acc. Chem. Res.* **2021**, *54* (24), 4530−4544.

(12) Gisbertz, S.; Reischauer, S.; Pieber, B. Overcoming limitations in dual photoredox/nickel-catalysed C-N cross-couplings due to catalyst deactivation. *Nat. Catal.* **2020**, *3* (8), 611−620.

(13) Crabtree, R. H. Deactivation in Homogeneous Transition Metal Catalysis: Causes, Avoidance, and Cure. *Chem. Rev.* **2015**, *115* (1), 127−150.

(14) Liu, J.; Chen, L.; Cui, H.; Zhang, J.; Zhang, L.; Su, C.-Y. Applications of metal-organic frameworks in heterogeneous supramolecular catalysis. *Chem. Soc. Rev.* **2014**, *43* (16), 6011−6061.
(15) Yaghi, O. M.; Kalmutzki, M. J.; Diercks, C. S. Building Units of MOFs. In *Introduction to Reticular Chemistry*; Wiley, 2019; pp 57−81.
(16) Furukawa, H.; Cordova, K. E.; O'Keeffe, M.; Yaghi, O. M. The Chemistry and Applications of Metal-Organic Frameworks. *Science* **2013**, *341* (6149), 1230444.
(17) Bavykina, A.; Kolobov, N.; Khan, I. S.; Bau, J. A.; Ramirez, A.; Gascon, J. Metal-Organic Frameworks in Heterogeneous Catalysis: Recent Progress, New Trends, and Future Perspectives. *Chem. Rev.* **2020**, *120* (16), 8468−8535.
(18) Zheng, H.; Fan, Y.; Song, Y.; Chen, J. S.; You, E.; Labalme, S.; Lin, W. Site Isolation in Metal-Organic Layers Enhances Photoredox Gold Catalysis. *J. Am. Chem. Soc.* **2022**, *144* (24), 10694−10699.
(19) Osadchii, D. Y.; Olivos-Suarez, A. I.; Szécsényi, C1.; Li, G.; Nasalevich, M. A.; Dugulan, I. A.; Crespo, P. S.; Hensen, E. J. M.; Veber, S. L.; Fedin, M. V.; Sankar, G.; Pidko, E. A.; Gascon, J. Isolated Fe Sites in Metal Organic Frameworks Catalyze the Direct Conversion of Methane to Methanol. *ACS Catal.* **2018**, *8* (6), 5542−5548.
(20) Wei, Y.-S.; Zhang, M.; Zou, R.; Xu, Q. Metal-Organic Framework-Based Catalysts with Single Metal Sites. *Chem. Rev.* **2020**, *120* (21), 12089−12174.
(21) Ji, P.; Manna, K.; Lin, Z.; Feng, X.; Urban, A.; Song, Y.; Lin, W. Single-Site Cobalt Catalysts at New Zr12(μ3-O)8(μ3-OH)8(μ2-OH)6 Metal-Organic Framework Nodes for Highly Active Hydrogenation of Nitroarenes, Nitriles, and Isocyanides. *J. Am. Chem. Soc.* **2017**, *139* (20), 7004−7011.
(22) Song, Y.; Li, Z.; Ji, P.; Kaufmann, M.; Feng, X.; Chen, J. S.; Wang, C.; Lin, W. Metal-Organic Framework Nodes Support Single-Site Nickel(II) Hydride Catalysts for the Hydrogenolysis of Aryl Ethers. *ACS Catal.* **2019**, *9* (2), 1578−1583.
(23) Sawano, T.; Lin, Z.; Boures, D.; An, B.; Wang, C.; Lin, W. Metal-Organic Frameworks Stabilize Mono(phosphine)-Metal Complexes for Broad-Scope Catalytic Reactions. *J. Am. Chem. Soc.* **2016**, *138* (31), 9783−9786.
(24) Feng, X.; Song, Y.; Li, Z.; Kaufmann, M.; Pi, Y.; Chen, J. S.; Xu, Z.; Li, Z.; Wang, C.; Lin, W. Metal-Organic Framework Stabilizes a Low-Coordinate Iridium Complex for Catalytic Methane Borylation. *J. Am. Chem. Soc.* **2019**, *141* (28), 11196−11203.
(25) Drake, T.; Ji, P.; Lin, W. Site Isolation in Metal-Organic Frameworks Enables Novel Transition Metal Catalysis. *Acc. Chem. Res.* **2018**, *51* (9), 2129−2138.
(26) Huang, Y.-B.; Liang, J.; Wang, X.-S.; Cao, R. Multifunctional metal-organic framework catalysts: synergistic catalysis and tandem reactions. *Chem. Soc. Rev.* **2017**, *46* (1), 126−157.
(27) Feng, X.; Song, Y.; Lin, W. Transforming Hydroxide-Containing Metal-Organic Framework Nodes for Transition Metal Catalysis. *Trends Chem.* **2020**, *2* (11), 965−979.
(28) Song, Y.; Feng, X.; Chen, J. S.; Brzezinski, C.; Xu, Z.; Lin, W. Multistep Engineering of Synergistic Catalysts in a Metal-Organic Framework for Tandem C-O Bond Cleavage. *J. Am. Chem. Soc.* **2020**, *142* (10), 4872−4882.
(29) Baek, J.; Rungtaweevoranit, B.; Pei, X.; Park, M.; Fakra, S. C.; Liu, Y.-S.; Matheu, R.; Alshmimri, S. A.; Alshehri, S.; Trickett, C. A.; Somorjai, G. A.; Yaghi, O. M. Bioinspired Metal-Organic Framework Catalysts for Selective Methane Oxidation to Methanol. *J. Am. Chem. Soc.* **2018**, *140* (51), 18208−18216.
(30) Mo, Q.; Zhang, L.; Li, S.; Song, H.; Fan, Y.; Su, C.-Y. Engineering Single-Atom Sites into Pore-Confined Nanospaces of Porphyrinic Metal-Organic Frameworks for the Highly Efficient Photocatalytic Hydrogen Evolution Reaction. *J. Am. Chem. Soc.* **2022**, *144* (49), 22747−22758.
(31) Zhu, Y.; Zheng, J.; Ye, J.; Cui, Y.; Koh, K.; Kovarik, L.; Camaioni, D. M.; Fulton, J. L.; Truhlar, D. G.; Neurock, M.; Cramer, C. J.; Gutiérrez, O. Y.; Lercher, J. A. Copper-zirconia interfaces in UiO-66 enable selective catalytic hydrogenation of CO2 to methanol. *Nat. Commun.* **2020**, *11* (1), 5849.
(32) Li, R.; Zhang, W.; Zhou, K. Metal-Organic-Framework-Based Catalysts for Photoreduction of CO2. *Adv. Mater.* **2018**, *30* (35), 1705512.
(33) Zhuo, T.-C.; Song, Y.; Zhuang, G.-L.; Chang, L.-P.; Yao, S.; Zhang, W.; Wang, Y.; Wang, P.; Lin, W.; Lu, T.-B.; Zhang, Z.-M. H-Bond-Mediated Selectivity Control of Formate versus CO during CO2 Photoreduction with Two Cooperative Cu/X Sites. *J. Am. Chem. Soc.* **2021**, *143* (16), 6114−6122.
(34) Zhu, Y.-Y.; Lan, G.; Fan, Y.; Veroneau, S. S.; Song, Y.; Micheroni, D.; Lin, W. Merging Photoredox and Organometallic Catalysts in a Metal-Organic Framework Significantly Boosts Photocatalytic Activities. *Angew. Chen., Int. Ed.* **2018**, *57* (43), 14090−14094.
(35) Frischmann, P. D.; Mahata, K.; Würthner, F. Powering the future of molecular artificial photosynthesis with light-harvesting metallosupramolecular dye assemblies. *Chem. Soc. Rev.* **2013**, *42* (4), 1847−1870.
(36) Mateo, D.; Morlanes, N.; Maity, P.; Shterk, G.; Mohammed, O. F.; Gascon, J. Efficient Visible-Light Driven Photothermal Conversion of CO2 to Methane by Nickel Nanoparticles Supported on Barium Titanate. *Adv. Funct. Mater.* **2021**, *31* (8), 2008244.
(37) Khan, I. S.; Mateo, D.; Shterk, G.; Shoinkhorova, T.; Poloneeva, D.; Garzón-Tovar, L.; Gascon, J. An Efficient Metal-Organic Framework-Derived Nickel Catalyst for the Light Driven Methanation of CO2. *Angew. Chen., Int. Ed.* **2021**, *60* (51), 26476−26482.
(38) Huang, H.-B.; Fang, Z.-B.; Wang, R.; Li, L.; Khanpour, M.; Liu, T.-F.; Cao, R. Engineering Hierarchical Architecture of Metal-Organic Frameworks for Highly Efficient Overall CO2 Photoreduction. *Small* **2022**, *18* (16), 2200407.
(39) Kundu, T.; Gilmanova, L.; Yong, W. F.; Kaskel, S. Metal-Organic Frameworks for Environmental Applications. In *Porous Materials: Theory and Its Application for Environmental Remediation*; Moreno-Piraján, J. C., Giraldo-Gutierrez, L., Gómez-Granados, F., Eds.; Springer International Publishing: Cham, Switzerland, 2021; pp 1−39.
(40) Park, J.; Lee, H.; Bae, Y. E.; Park, K. C.; Ji, H.; Jeong, N. C.; Lee, M. H.; Kwon, O. J.; Lee, C. Y. Dual-Functional Electrocatalyst Derived from Iron-Porphyrin-Encapsulated Metal-Organic Frameworks. *ACS Appl. Mater. Interfaces* **2017**, *9* (34), 28758−28765.
(41) Stanley, P. M.; Su, A. Y.; Ramm, V.; Fink, P.; Kimna, C.; Lieleg, O.; Elsner, M.; Lercher, J. A.; Rieger, B.; Warnan, J.; Fischer, R. A. Photocatalytic CO2-to-Syngas Evolution with Molecular Catalyst Metal-Organic Framework Nanozymes. *Adv. Mater.* **2023**, *35* (6), 2207380.
(42) Peralta, R. A.; Huxley, M. T.; Lyu, P.; Díaz-Ramírez, M. L.; Park, S. H.; Obeso, J. L.; Leyva, C.; Heo, C. Y.; Jang, S.; Kwak, J. H.; Maurin, G.; Ibarra, I. A.; Jeong, N. C. Engineering Catalysis within a Saturated In(III)-Based MOF Possessing Dynamic Ligand-Metal Bonding. *ACS Appl. Mater. Interfaces* **2023**, *15* (1), 1410−1417.
(43) Lan, G.; Fan, Y.; Shi, W.; You, E.; Veroneau, S. S.; Lin, W. Biomimetic active sites on monolayered metal-organic frameworks for artificial photosynthesis. *Nat. Catal.* **2022**, *5* (11), 1006−1018.
(44) Lan, G.; Quan, Y.; Wang, M.; Nash, G. T.; You, E.; Song, Y.; Veroneau, S. S.; Jiang, X.; Lin, W. Metal-Organic Layers as Multifunctional Two-Dimensional Nanomaterials for Enhanced Photoredox Catalysis. *J. Am. Chem. Soc.* **2019**, *141* (40), 15767−15772.
(45) Wu, Q.-J.; Liang, J.; Huang, Y.-B.; Cao, R. Thermo-, Electro-, and Photocatalytic CO2 Conversion to Value-Added Products over Porous Metal/Covalent Organic Frameworks. *Acc. Chem. Res.* **2022**, *55* (20), 2978−2997.
(46) Liu, J.; Fan, Y.-Z.; Zhang, K.; Zhang, L.; Su, C.-Y. Engineering Porphyrin Metal-Organic Framework Composites as Multifunctional Platforms for CO2 Adsorption and Activation. *J. Am. Chem. Soc.* **2020**, *142* (34), 14548−14556.
(47) Cadiau, A.; Kolobov, N.; Srinivasan, S.; Goesten, M. G.; Haspel, H.; Bavykina, A. V.; Tchalala, M. R.; Maity, P.; Goryachev, A.; Poryvaev, A. S.; Eddaoudi, M.; Fedin, M. V.; Mohammed, O. F.;

Gascon, J. A Titanium Metal-Organic Framework with Visible-Light-Responsive Photocatalytic Activity. *Angew. Chen., Int. Ed.* **2020**, *59* (32), 13468−13472.
(48) Huang, J.-N.; Dong, Y.-J.; Zhao, H.-B.; Chen, H.-Y.; Kuang, D.-B.; Su, C.-Y. Efficient encapsulation of CsPbBr3 and Au nanocrystals in mesoporous metal-organic frameworks towards synergetic photocatalytic CO2 reduction. *Journal of Materials Chemistry A* **2022**, *10* (47), 25212−25219.
(49) Wang, J.-L.; Wang, C.; Lin, W. Metal-Organic Frameworks for Light Harvesting and Photocatalysis. *ACS Catal.* **2012**, *2* (12), 2630−2640.
(50) Wang, C.; Xie, Z.; deKrafft, K. E.; Lin, W. Doping Metal-Organic Frameworks for Water Oxidation, Carbon Dioxide Reduction, and Organic Photocatalysis. *J. Am. Chem. Soc.* **2011**, *133* (34), 13445−13454.
(51) Guo, S.; Kong, L.-H.; Wang, P.; Yao, S.; Lu, T.-B.; Zhang, Z.-M. Switching Excited State Distribution of Metal-Organic Framework for Dramatically Boosting Photocatalysis. *Angew. Chen., Int. Ed.* **2022**, *61* (30), No. e202206193.
(52) Yin, H.-Q.; Zhang, Z.-M.; Lu, T.-B. Ordered Integration and Heterogenization of Catalysts and Photosensitizers in Metal-/Covalent-Organic Frameworks for Boosting CO2 Photoreduction. *Acc. Chem. Res.* **2023**, *56* (19), 2676−2687.
(53) Yan, Z.-H.; Du, M.-H.; Liu, J.; Jin, S.; Wang, C.; Zhuang, G.-L.; Kong, X.-J.; Long, L.-S.; Zheng, L.-S. Photo-generated dinuclear {Eu(II)}2 active sites for selective CO2 reduction in a photosensitizing metal-organic framework. *Nat. Commun.* **2018**, *9* (1), 3353.
(54) Wu, D.; Yin, H.-Q.; Wang, Z.; Zhou, M.; Yu, C.; Wu, J.; Miao, H.; Yamamoto, T.; Zhaxi, W.; Huang, Z.; Liu, L.; Huang, W.; Zhong, W.; Einaga, Y.; Jiang, J.; Zhang, Z.-M. Spin Manipulation in a Metal-Organic Layer through Mechanical Exfoliation for Highly Selective CO2 Photoreduction. *Angew. Chen., Int. Ed.* **2023**, *62* (18), No. e202301925.
(55) Pan, Z.-H.; Weng, Z.-Z.; Kong, X.-J.; Long, L.-S.; Zheng, L.-S. Lanthanide-containing clusters for catalytic water splitting and CO2 conversion. *Coord. Chem. Rev.* **2022**, *457*, 214419.
(56) Bloch, E. D.; Britt, D.; Lee, C.; Doonan, C. J.; Uribe-Romo, F. J.; Furukawa, H.; Long, J. R.; Yaghi, O. M. Metal Insertion in a Microporous Metal-Organic Framework Lined with 2,2′-Bipyridine. *J. Am. Chem. Soc.* **2010**, *132* (41), 14382−14384.
(57) Yildiz, C.; Kutonova, K.; Oßwald, S.; Titze-Alonso, A.; Bitzer, J.; Bräse, S.; Kleist, W. Post-synthetic Modification of DUT-5-based Metal Organic Frameworks for the Generation of Single-site Catalysts and their Application in Selective Epoxidation Reactions. *ChemCatChem.* **2020**, *12* (4), 1134−1142.
(58) Senkovska, I.; Hoffmann, F.; Fröba, M.; Getzschmann, J.; Böhlmann, W.; Kaskel, S. New highly porous aluminium based metal-organic frameworks: Al(OH)(ndc) (ndc = 2,6-naphthalene dicarboxylate) and Al(OH)(bpdc) (bpdc = 4,4′-biphenyl dicarboxylate). *Microporous Mesoporous Mater.* **2009**, *122* (1), 93−98.
(59) Wang, Z.; Yeary, P.; Feng, X.; Lin, W. Self-adaptive Metal-Organic Framework Assembles Di-iron Active Sites to Mimic Monooxygenases. *J. Am. Chem. Soc.* **2023**, *145* (15), 8647−8655.
(60) Guo, Q.-Y.; Wang, Z.; Feng, X.; Fan, Y.; Lin, W. Generation and Stabilization of a Dinickel Catalyst in a Metal-Organic Framework for Selective Hydrogenation Reactions. *Angew. Chen., Int. Ed.* **2023**, *62* (35), No. e202306905.
(61) Hoon-Khosla, M.; Fawcett, W. R.; Goddard, J. D.; Tian, W.-Q.; Lipkowski, J. Reflection FTIR Studies of the Conformation of 2,2‘-Bipyridine Adsorbed at the Au(111) Electrode/Electrolyte Interface. *Langmuir* **2000**, *16* (5), 2356−2362.
(62) Colpas, G. J.; Maroney, M. J.; Bagyinka, C.; Kumar, M.; Willis, W. S.; Suib, S. L.; Mascharak, P. K.; Baidya, N. X-ray spectroscopic studies of nickel complexes, with application to the structure of nickel sites in hydrogenases. *Inorg. Chem.* **1991**, *30* (5), 920−928.
(63) Schmid, B.; Garces, F. O.; Watts, R. J. Synthesis and characterizations of cyclometalated iridium(III) solvento complexes. *Inorg. Chem.* **1994**, *33* (1), 9−14.
(64) Choy, J.-H.; Hwang, S.-H.; Yoon, J.-B.; Chin, C.-S.; Oh, M.; Lee, H. X-ray absorption spectroscopic studies on the iridium(III) complexes. *Mater. Lett.* **1998**, *37* (3), 168−175.
(65) Lowry, M. S.; Goldsmith, J. I.; Slinker, J. D.; Rohl, R.; Pascal, R. A.; Malliaras, G. G.; Bernhard, S. Single-Layer Electroluminescent Devices and Photoinduced Hydrogen Production from an Ionic Iridium(III) Complex. *Chem. Mater.* **2005**, *17* (23), 5712−5719.

https://doi.org/10.1021/acscatal.4c02326
ACS Catal. 2024, 14, 9217−9223